1 **IL-1α secreted by subcapsular sinus macrophages promotes melanoma**

2 **metastasis in the sentinel lymph node by upregulating STAT3 signaling in**

3 **the tumor.**

4 *Tommaso Virgilio[1,2], Joy Bordini[1,3], Giulio Sartori[4], Irene Latino[1], Daniel Molina-Romero[1,5], Cristina*

5 *Leoni[1], Murodzhon Akhmedov[1,6], Andrea Rinaldi[4], Alberto J. Arribas[4], Diego Morone[1], S. Morteza*

6 *Seyed Jafari[7], Marina Bersudsky[8], Aner Ottolenghi[8], Ivo Kwee[1,6], Anna Maria Chiaravalli[9], Fausto*

7 *Sessa[9], Robert E. Hunger[7], Antonino Bruno[10], Lorenzo Mortara[11], Elena Voronov[8], Silvia Monticelli[1],*

8 *Ron N. Apte[8], Francesco Bertoni[4,12], Santiago F. Gonzalez[1*]*

9 *1: Institute for Research in Biomedicine, Università della Svizzera Italiana, Bellinzona, Switzerland.*

10 *2: Graduate School for Cellular and Biomedical Sciences, University of Bern, Bern, Switzerland.*

11 *3: Genomsys SA, Lugano, Switzerland.*

12 *4: Institute of Oncology Research, Università della Svizzera Italiana, Bellinzona, Switzerland.*

13 *5: Graduate School Ecole Polytechnique Fédérale de Lausanne, Lausanne, Switzerland.*

14 *6: BigOmics Analytics, Lugano, Switzerland.*

15 *7: Department of Dermatology, Inselspital, Bern University Hospital, University of Bern, Bern, Switzerland.*

16 *8: The Shraga Segal Department of Microbiology, Immunology and Genetics, Faculty of Health Sciences, Ben-*

17 *Gurion University of the Negev, Beer Sheva, Israel.*

18 *9: Unit of Pathology, ASST dei Sette Laghi, Department of Medicine and Surgery, University of Insubria, Varese,*

19 *Italy*

20 *10: Laboratory of Innate Immunity, Unit of Molecular Pathology, Biochemistry, and Immunology, IRCCS*

21 *MultiMedica, Milan, Italy.*

22 *11: Laboratory of Immunology and General Pathology, Department of Biotechnology and Life Sciences, University*

23 *of Insubria, Varese, Italy*

24 *12: Oncology Institute of Southern Switzerland (IOSI), Bellinzona, Switzerland*

25

26

27

28

29

30

31

32

33

34 **Corresponding Author:**

35 *Santiago Fernandez Gonzalez*

36 *Institute for Research in Biomedicine, via Vincenzo Vela 6.*

37 *CH-6500 Bellinzona. Switzerland*

38 *Tel: (+41) 91 8200 360*

39 *Email: santiago.gonzalez@irb.usi.ch*

ABSTRACT

During melanoma metastasization, tumor cells originated in the skin migrate via lymphatic vessels to the sentinel lymph node (sLN) in a process that facilitates their spread across the body. Here, we characterized the innate inflammatory responses to melanoma metastasis in the sLN. For this purpose, we confirmed the migration of fluorescent metastatic melanoma cells to the sLN and we characterized the inflammatory response in the metastatic microenvironment. We found that macrophages located in the subcapsular sinus (SSM), produce pro-tumoral IL-1α after recognition of tumor antigens. Moreover, we confirmed that the administration of an anti-IL-1α depleting antibody reduced metastasis. Conversely, the administration of recombinant IL-1α accelerated the lymphatic spreading of the tumor. Additionally, the elimination of the macrophages significantly reduced the progression of the metastatic spread. To understand the mechanism of action of IL-1α in the context of the lymph node microenvironment, we applied single-cell RNA sequencing to dissected metastases obtained from animals treated with an anti-IL-1α blocking antibody. Amongst the different pathways affected, we identified STAT3 as one of the main targets of IL-1α signaling in metastatic cells. Moreover, we found that the anti-IL-1α anti-tumoral effect was not mediated by lymphocytes, as IL-1R1 KO mice did not show any improvement in metastasis growth. Finally, we found a synergistic anti-metastatic effect of the combination of IL-1α blocking and the STAT3 inhibitor (STAT3i) stattic. In summary, we described a new mechanism by which SSM support melanoma metastasis, highlighting a new target for immunotherapy.

KEYWORDS: *Melanoma, Metastasis, Sentinel Lymph Node, IL-1α, STAT3, Macrophages, Subcapsular sinus, Immunotherapy, Inflammation.*

1

65 **INTRODUCTION**

66 Melanoma is the most lethal form of skin cancer and a serious threat for public health. In recent
67 years, the incidence of this type of cancer has progressively increased and it is currently one
68 of the most common malignancies in both adult and young individuals[1]. During melanoma
69 development, malignant cells in the skin acquire genetic mutations that lead them towards the
70 lymphatic vessels, which serve as a transportation system[2]. Once in the lymphatics, the
71 metastatic cells initiate an active migration that leads them towards the sentinel LN (sLN)[3].
72 The presence of melanoma metastasis in this organ is indicative of a poor prognosis,
73 drastically decreasing the survival rate of the patients[4,5].

74

75 Upon breaching the LN capsule, metastatic cells access the LN sinuses via the afferent
76 lymphatics, following chemokine gradients generated by lymphatic endothelial cells[6–8]. The
77 invasion of the sLN is initiated in the subcapsular sinus area (SS)[6,8,9] and progressively
78 spreads towards the inner structures of the sLN[10]. This process facilitates the access of the
79 metastatic cells to the bloodstream via high-endothelial venules (HEVs) and their consequent
80 spread to distant organs[11–13].

81

82 The LN sinuses are populated by resident phagocytic cells, including three distinct
83 macrophage subsets called subcapsular sinus macrophages (SSM), medullary macrophages
84 (MM) and medullary cord macrophages (MCM), according to the area they reside[14].
85 Strategically positioned along the SS area, SSM are the first immune cells to encounter lymph-
86 transported antigens and pathogens, preventing their systemic dissemination[15]. In addition,
87 they play a critical role in the initiation of the immune responses against immune complexes
88 and virus[16–18] as well as promoting humoral immunity[19,20]. Despite the role of macrophages
89 against infectious pathogens has been largely demonstrated, their involvement in the
90 response against tumor remains somehow controversial[21–27]. This is mainly due to the ability
91 of these cells to activate either anti- or pro-tumoral responses, according to their cell plasticity,
92 that allows them being dicotomically classified in M1 and M2 macrophages[28,29]. For instance,
93 some authors have described a protective function of SSM, which was associated with the
94 capturing of dead tumor cell-derived antigens[23] and their cross-presentation to CD8+ T cells[21].
95 Moreover, Tacconi and colleagues have recently suggested a protective role of CD169+ LN
96 macrophages in breast cancer metastasis, which was dependent on the presence of B cells[27].
97 Conversely, other studies have revealed a pro-tumoral effect of these cells, mainly linked with
98 their capacity to trigger and maintain the inflammatory response both in peripheral and
99 lymphoid tissues[9,30,31].

100

101　The inflammatory response plays a fundamental role in the behavior of cancer cells. Some

102　cancers, including melanoma, are able indeed to grow in chronically inflamed conditions and

103　to take advantage of inflammation[32–35]. One of the mechanisms by which innate inflammation

104　supports tumor growth is by the release of IL-1 family cytokines[36,37]. IL-1β, the major

105　component of this family, has been shown to endorse different tumors, mainly by mediating

106　immune suppression and by activating endothelial cells[38,39]. Indeed, recent evidence suggests

107　that blocking the IL-1R signaling might prolong the survival time of patients with different

108　tumors[40–44]. In addition, IL-1β antagonism can synergize with immune checkpoint inhibitor

109　therapy[38]. However, the mechanisms responsible for this process might vary between the

110　primary tumor and the metastatic areas, including the sLN[45,46]. Understanding these

111　differences will influence the design of specific immunotherapies intended to control tumor

112　dissemination in both locations[47,48] and in different types of tumors, including melanoma[49,50].

113

114　In the present work we characterized the innate immune response of the sLN to melanoma

115　metastasis invasion. Furthermore, we identified a novel mechanism that associates the

116　inflammatory reaction, initiated by SSM, to the progression of the metastatic melanoma cells.

117　These results will have a potential impact generating new therapies and improving the

118　efficiency of the current immunotherapies against metastatic melanoma, possibly acting on

119　macrophages, that represent the most abundant inflammatory cells infiltrating tumor.

3

120   **RESULTS**

121   ***Development and characterization of a murine model of melanoma metastasis in the***

122   ***draining popliteal lymph node.*** To study the metastatic process in the sentinel lymph node

123   (sLN) we transduced the melanoma cell line B16-F1 with a lentiviral vector codifying for

124   mCherry and we characterized the expression of this fluorescent protein by FACS and

125   microscopy (Fig. 1A and Supp. Fig. 1A, respectively). The primary tumor was induced by

126   subcutaneous injection of the cancer cells in the mouse footpad, similarly to what was

127   previously reported (Fig. 1B)[51]. Next, the formation of the primary tumor was monitored by

128   measuring tumor volume (Supp. Fig. 1B,C) and tumor fluorescence was quantified by using

129   the *In Vivo* Imaging System (IVIS; Fig. 1C,D). Following this approach, we observed a

130   significant engraftment starting from week one post tumor implantation (p.t.i) (Fig. 1D).

131   Subsequently, we identified macrometastases in the sLN at three weeks p.t.i. (Fig. 1E). To

132   study in more detail the progression of melanoma cells towards the sLN, we employed flow

133   cytometry, observing a significant increase of the metastatic cells at day 15 p.t.i. compared to

134   control samples (Fig 1F). In addition, to characterize the area of the metastasis, we used

135   confocal microscopy analysis of the sLN at different time points following tumor induction (Fig.

136   1G). We measured a significant increase in the metastatic area starting at two weeks (Fig.

137   1H). Besides, the morphology of sLN metastases showed that, in concordance with previous

138   works in humans[8], metastatic cells initially invade the subcapsular sinus area (SS) (Fig. 1G,I).

139   Furthermore, at later time points, the metastasis progressively expanded through the

140   interfollicular area (IF), invading the transverse sinus (Fig. 1I, Sup Fig. 1D). Conversely, we

141   did not observe the presence of metastatic cells in distant organs, such as the spleen or the

142   lungs, at equivalent time points (Fig. 1J), confirming the lymphatic dissemination of the tumor.

143

144   ***IL-1α promotes melanoma growth in the sLN.*** To characterize the inflammatory reaction

145   induced by metastasis development, we quantified the total number of immune cells infiltrated

146   in the sLN, observing a significant two-fold increase starting from the first week p.t.i. (Fig. 2A).

147   More in detail, increases in dendritic cells (MHC-II$^+$, CD11c^{high}, CD11b$^+$ and CD11b$^-$), NK cells

148   (CD3$^-$, NK1.1$^+$), neutrophils (MHC-II$^-$, GR1^{high}), monocytes (MHC-II$^-$, GR1^{int}) and macrophages

149   (MHC-II$^+$, CD11c^{intlow}, CD11b$^+$, Supp. Fig. 2A), as well as B (B220$^+$) and T cells (CD4$^+$, CD8$^+$,

150   and FOXP3$^+$ T$_{reg}$), were observed (Supp. Fig. 2B). To further characterize the recruitment of

151   immune cells to the metastasized sLN, a multiplexed approach was applied to quantify the

152   concentration of different inflammatory chemokines, including CXCL13, CXCL9, CCL22,

153   CCL5 and CCL2, in the sLN supernatant, observing a significant increase at week three p.t.i.

154   (Supp. Fig. 2C). Additionally, we measured the concentration of other 13 inflammatory

155   cytokines. Among the molecules analyzed, IL-1α exhibited a significant increase at week three

156 p.t.i., compared to the control group. (Fig. 2B). A further study of the dynamics of IL-1α release

157 highlighted that the upregulation started at week two p.t.i. (Fig. 2C). To evaluate if IL-1α

158 secretion was associated with other tumor models, including another solid tumor infiltrating

159 the sLN, we measured the level of this cytokine in sLN metastasized with melanoma B16-F10,

160 or with the breast cancer cell line E0771, observing similar levels of IL-1α in both models at

161 three weeks p.t.i. (Fig. 2D).

162 Next, we hypothesized a pro-tumoral role of IL-1α in the metastatic context. To explore this

163 hypothesis, we treated mice with a daily subcutaneous injection of either IL-1α depleting

164 antibody or recombinant IL-1α protein. Interestingly, blocking the IL-1α pathway by

165 administration of the neutralizing antibody significantly decreased the metastasis growth in the

166 sLN, as indicated by a reduction in the number of metastatic cells measured by flow cytometric

167 analysis at week three p.t.i.. Conversely, the number of melanoma cells significantly increased

168 in the sLN treated with recombinant IL-1α at equivalent time points (Fig. 2E). Moreover, the

169 metastatic ratio, defined as the number of mice developing sLN metastasis at week three p.t.i.

170 divided by the total number of mice showing primary tumor engraftment, was higher in the

171 animals treated with recombinant IL-1α and it was reduced following IL-1α depletion (Fig. 2F).

172 Nevertheless, the observed variation in the metastasis size after treatment could be

173 dependent on the size of the primary tumor. Therefore, to discard that possibility, we

174 normalized the number of metastatic cells to the primary tumor volume, confirming the results

175 previously observed in Fig. 2E (Supp. Fig. 2D). Additionally, the previously described

176 treatments did not have a significant effect on the growth of the primary tumor in comparison

177 to the untreated control group (Supp. Fig. 2E). However, we observed that IL-1α KO mice

178 showed a reduction not only of the metastatic cells at week three p.t.i. (Fig. 2G), but also of

179 the primary tumor volume starting from the fourth week p.t.i. (Supp. Fig. 2F). This discrepancy

180 could be partially explained by the mode of administration of the treatment, which promotes

181 the transport towards the draining lymphatics, or by the time of administration of the

182 compounds in comparison to the constant absence of IL-1α in the tumor microenviroment in

183 KO mice.

184

185 ***Subcapsular sinus macrophages are the main source of pro-tumoral IL-1α and***

186 ***disappear after tumor phagocytosis.*** In a previous study we characterized the role of LN

187 macrophages as the main producers of IL-1α in the LN, following influenza vaccination[20]. To

188 elucidate the main source of IL-1α in the melanoma model, we analyzed the infiltrating immune

189 cells from the metastatic regions of the LN, by single cell RNA sequencing (scSeq, Fig. 3A).

190 Following this approach, we confirmed that LN macrophages are the main producers of IL-1α

191 (Fig. 3 B, C). Moreover, the depletion of this population, following the injection with clodronate

192   liposomes (CLL), significantly reduced the levels of IL-1α in the LN supernatant (Fig 3D).
193   Importantly, depletion of macrophages following CLL administration completely abrogated the
194   growth of the metastatic melanoma cells in the LN, confirming their pro-tumoral nature (Supp.
195   Fig. 3A, B). However, the local administration of CLL did not affect the volume of the primary
196   tumor (Supp. Fig 3C). Next, to identify the specific subset of macrophages responsible for the
197   production of IL-1α, we used flow cytometry (Fig. 3E, F) and confocal microscopy (Fig. 3G),
198   which pointed out SSM (CD169^{+}, F4/80^{-}) as the main source of IL-1α in the metastatic region.
199   To prove the relevance of these findings also in humans, we performed immunohistochemical
200   staining of melanoma metastatic LN from patients, confirming that the local production of IL-
201   1α was associated with CD68^{+} tumor infiltrated macrophages in the SS region (Supp. Fig. 3D).
202   As suggested by other studies[23], we also reported that tumor infiltrating SSM phagocyte
203   melanoma cells (Fig. 3G, H, Supp. Fig. 3E, Supp. Mov. 1).

204   To investigate the mechanism of release of IL-1α by SSM, we quantified cell numbers by flow
205   cytometry, observing that the total number of SSM remained constant during the first three
206   weeks p.t.i. (Supp. Fig. 3F), while their frequency decreased (Supp. Fig. 3G). This was in
207   contrast with a significant increase in the total number of macrophages observed at equivalent
208   time points (Supp. Fig. 2A). Therefore, to investigate if SSM disappear following metastasis
209   growth, we quantified by confocal microscopy the expression of the macrophage marker
210   CD169 in different regions of the metastatic sLN. Interestingly, we observed that the CD169
211   layer in the SS was absent in the proximity of the metastatic area (Fig. 3I). More in detail,
212   CD169 in the SS surrounding the metastatic region was expressed significantly less than in
213   the non-metastasized SS (Fig. 3J), suggesting that SSM in direct contact with melanoma might
214   undergo a cell death process. To confirm that the phagocytosis of tumor cell debris was able
215   to induce SSM disappearance we injected B16-F1 lysate in the mouse footpad and performed
216   flow cytometric analysis at 12 and 24 h following injection. We observed that the percentage
217   of SSM significantly decreased compared with non-injected controls (Supp. Fig. 3H).

218

219   ***SSM-derived IL-1α induces melanoma proliferation.***

220   In previous studies, we have demonstrated the involvement of IL-1α in the inflammatory
221   reaction in the LN[20,52]. However, we did not observe here any significant effect in the
222   recruitment of the major immune cells subtypes in the sLN following treatment with anti-IL-1α
223   (Supp. Fig. 4 A, B). To further characterize the pro-tumoral mechanism of IL-1α, we measured
224   the expression of IL-1R1, the only known receptor involved in the signaling of IL-1α[39], in the
225   infiltrated cell types of a metastatic sLN. Amongst the evaluated cells, NK cells and melanoma
226   displayed the highest level of IL-1R1 expression (Fig. 4A). To clarify the role of immune cells
227   in mediating the pro-tumoral function of IL-1α, we induced melanoma in IL-1R1 KO mice, in

228 which tumor microenvironment cells can't be involved in IL-1 signaling and only the tumor cells

229 express this receptor. The absence of IL-1R1 in the immune compartment did not significantly

230 affect neither the metastasis growth in the sLN (Fig. 4B) nor the metastatic ratio (Fig. 4C),

231 demonstrating that the pro-tumoral effect of IL-1 signaling was not associated with the immune

232 cell response. Next, after confirming the expression of IL-1R1 in cultured melanoma cells

233 (Supp. Fig. 4C), we measured their proliferation rate following exposure to IL-1α. We

234 discovered that IL-1α significantly promoted the proliferation of melanoma in murine and

235 human cell lines (Fig. 4D and 4E, respectively). To further characterize the activation of IL-

236 1R1 signaling in B16-F1 melanoma cells, we measured by qPCR the expression of the gene

237 codifying for the Myeloid Differentiation Primary Response 88 protein (MYD88), the main

238 mediator of the Interleukin-1 receptor associated kinase (IRAK) signaling activated by IL-

239 1R1[39]. The results confirmed that melanoma cells treated with recombinant IL-1α significantly

240 upregulated the *Myd88* gene (Fig. 4F).

241

242 ***IL-1α promotes aggressiveness of melanoma metastasis via STAT3.*** To study the

243 pathways influenced by IL-1α blocking *in vivo*, we performed scSeq of dissected metastases

244 from mice treated with anti-IL-1α antibody at three weeks p.t.i. (Supp. Fig. 5A). Next, we

245 performed an influence analysis on the transcriptomic scSeq data (Fig. 5A) to identify the top

246 ten IL-1α key players, defined as the genes with the highest influence from all the *il1a* related

247 pathways (Fig. 5B). Amongst them, we focused on *STAT3*, which was the most differentially

248 expressed gene among the *il1a* key players following IL-1α depletion (Fig. 5C). This gene

249 codifies for the transcription factor STAT3, a well characterized mediator of aggressiveness in

250 different cancers, including melanoma[53,54]. Furthermore, scSeq analysis of STAT3 expression

251 highlighted the metastatic melanoma as the cells exhibiting the highest expression levels of

252 this transcription factor (Fig. 5D). Moreover, the induction of the *STAT3* gene in melanoma

253 cells by IL-1α was confirmed *in vitro* by the administration of recombinant IL-1α (Fig. 5E). To

254 recapitulate this mechanism at a functional level, we studied STAT3 protein expression and

255 phosphorylation in murine melanoma cells using immunoblot assay. Treatment with

256 recombinant IL-1α induced a significant overexpression of STAT3 in comparison to untreated

257 controls starting at 24 h post IL-1α administration, while the addition of the anti-IL-1α depleting

258 antibody reverted this phenotype (Fig. 5F). Furthermore, exposure to recombinant IL-1α

259 induced the phosphorylation of STAT3, which was prevented by the depletion treatment (Fig.

260 5G). To evaluate if this mechanism was also present in a human model, we quantified STAT3

261 and pSTAT3 in the A375 cell line post administration of human recombinant IL-1α, and we

262 observed a significant increase of both total and phosphorylated forms in comparison to

263 untreated controls (Fig. 5H and 5I, respectively). Moreover, IHC sections of sLN from human

7

264 patients confirmed the expression and phosphorylation of STAT3 in the metastatic lesions
265 (Supp. Fig. 5B, C). Once we confirmed the connection between IL-1α and STAT3, we
266 evaluated if a therapy with a STAT3 inhibitor (STAT3i) was able to improve the efficiency of
267 the previously described IL-1α blocking therapy in the model of metastatic melanoma. Firstly,
268 we observed that the administration of the combined therapies *in vivo* was able to contain the
269 growth of the metastases more effectively than each of the two individual treatments (Fig. 5J).
270 Additionally, we evaluated the combinatorial effect of these two therapies using an *in vitro*
271 system, which highlighted a synergistic effect of the anti-IL-1α blocking therapy combined with
272 the STAT3i stattic (Fig. 5K, Supp. Fig. 5D, E). In more detail, the addition of stattic improved
273 both the efficacy (Supp. Fig. 5F) and the potency (Supp. Fig. 5G, H) of the IL-1α blocking
274 therapy.

275

276 **DISCUSSION**

277 In the present work, we characterized the innate immune responses of the sLN to melanoma
278 metastasis invasion. We discovered that the SSM, which are the first immune cells to
279 encounter melanoma metastasis in the sLN, phagocyted malignant cells and released IL-1α.
280 Rather than triggering a tumor-killing inflammation, this cytokine increased metastatic cells
281 aggressiveness by promoting STAT3 phosphorylation and increasing cancer proliferation.
282 Importantly, blocking IL-1α decreased metastatic growth and cooperated synergistically with
283 STAT3 inhibition.

284

285 STAT3 is a transcriptional factor with a relevant role in melanoma progression[55], together with
286 relevant immunosuppressive and pro-angiogenic properties[56,57]. Diverse studies investigated
287 the STAT3 pathway and its activation by IL-6[58]. Of note, no studies reported similar effects of
288 IL-1α. Based on this gap of knowledge, we stress a new target for metastatic melanoma
289 therapy, acting on STAT3 signaling. This finding has further relevance in the context of
290 combined therapies, which represent a very promising approach to target cancer cells at
291 different levels, including tumor microenvironment[59,60]. In this context, blocking multiple
292 immune pathways, such as IL-1α and IL-6, might improve the efficacy of STAT3i in comparison
293 to single or dual therapy, as suggested by other studies indicating the synergistic effect of
294 these two cytokines[36]. In addition, considering the variability of cytokines levels and responses
295 to cytokines-based therapies in patients[61], IL-1α blockade could be envisaged as an
296 alternative to IL-6 inhibition for boosting STAT3i[62] in those patients with low levels of IL-6 and
297 low sensitivity to IL-6 depletion[63]. The specific cytokines expression profiling in patients, in
298 fact, might be a useful tool to predict the patient response to the treatment and to design the
299 best therapeutic strategy, according to the concept of personalized medicine, as previously

300   proposed[64–66]. Moreover, IL-1α blocking agents have already been tested in clinical trials on

301   patients with various tumors and with different grading, showing variable efficiency[41,42,44,64].

302   Moreover, previous evidence, described a possible connection between PD-1 and IL-1[38,67] or

303   STAT3[57,68] in various tumors, indicating that IL-1α blockade in combination with other

304   therapies, including checkpoint inhibitors, might be object of further studies.

305   Another important aspect of the present work is the focus on metastasization. Metastases are

306   in fact more dangerous than primary tumors for patients, especially in melanoma[69]. Moreover,

307   their biology might differ substantially from the primary tumor[70]. For instance, STAT3 favors

308   the spread of melanoma cells to distant organs, and it is particularly expressed in the

309   melanoma metastasis[53,54]. For this reason, the identification of the IL-1α – STAT3 axis, able

310   to address efficiently metastases at their first stage, gains particular clinical relevance[48,71].

311   Furthermore, the pro-tumoral effect of SSM over the metastatic melanoma might be

312   associated with the more aggressive phenotype acquired by these cells in comparison to the

313   primary tumor or to peripheral blood circulating melanoma cells[11,12]. However, other

314   mechanisms, such as, for instance, the lymph-mediated protection from ferroptosis[13], are also

315   involved in this process.

316

317   In this study, we clearly characterized the pro-tumoral activity of SSM during melanoma

318   metastasis. However, previous evidence reported controversial functions of SSM in tumor

319   biology[9,25,72]. These cells, indeed, belong to the family of macrophages, which are capable of

320   activating both pro- and anti- tumoral mechanisms, as a consequence of their cellular

321   plasticity[73]. For this reason, targeting a specific pathway, as we proposed here, might reveal

322   a better strategy than depleting the whole macrophage population, avoiding the hampering of

323   possible anti-metastatic functions of these cells[23,24,74]. Similarly, the development of drugs

324   capable of targeting specifically SSM might reveal useful to block the IL-1α – STAT3 axis only

325   in these cells and to boost their anti-tumoral properties, in a process of macrophages re-

326   polarization[75]. Unfortunately, despite recent studies described compounds capable of

327   localizing differentially in the SCS and in the medullary area of the LN, a therapy able to

328   differentiate specifically macrophage subsets in the LN is still missing [72,76,77].

329

330   Additionally, SSM initiate the inflammatory response in the sLN by different mechanisms,

331   including cell death associated with the release of pre-stored IL-1α[20,78], which functions as an

332   alarmin molecule following release from dying cells[79]. However, despite we observed a

333   prominent recruitment of immune cells, we have not detected an efficient tumor-killing.

334   Different hypotheses could explain this observation, including but not limiting to the exhaustion

335   of the innate immunity, a higher affinity for IL-1α in melanoma cells in comparison to immune

9

336   cells, or a specific inhibition of IL-1R1 by IL-1R antagonist in the immune compartment, which

337   has been previously suggested in a study in human patients[80]. These and other hypotheses

338   will furnish exciting insights on novel methods to improve immunotherapy and should be

339   investigated in the future.

340

341   In conclusion, our results provide evidence of a novel function of SSM in melanoma metastasis

342   progression by controlling the IL-1α – STAT3 axis. Importantly, IL-1α blocking decreased

343   metastasis growth and acted synergistically with a STAT3i in controlling tumor growth. Taken

344   together, these findings provide with new opportunities to improve currently available

345   immunotherapies against metastatic melanoma.

10

MATERIALS AND METHODS

Cell culture and lentiviral transduction

B16-F1, B16-F10 and A375 cell lines were provided, respectively, by G. Guarda (IRB, Bellinzona) and C. Catapano (IOR, Bellinzona). E0771 cell lines were acquired from Ch3 BioSystems. All cell lines were maintained in a complete RPMI medium (RPMI+Hepes, 10 % heat inactivated FBS, 1 % Glutamax, 1 % sodium pyruvate, 1 % non-essential amino acids, 50 units/mL Penicillin, 50 µg/mL Streptomycin and 50 µM β-mercaptoethanol) and regularly tested for mycoplasma (MycoAlert Mycoplasma Detection kit, Lonza). The B16-F1-mCherry and B16-F1-Azurite cell lines were generated by lentiviral transduction. Briefly, lentiviral plasmids pSicoR-Ef1a-mCh (Addgene 31847) or pLV-Azurite (Addgene 36086) were transfected in HEK293T cells with packaging vectors pMD2G and psPAX (Addgene 12260 and 12259) to generate viral particles. After concentration by centrifugation, the virus was later collected and used for B16-F1 transduction. Transduced fluorescent cells were selected by live cells sorting using BD FACSAria Sorter.

Mice

The Institute for Research in Biomedicine (IRB) hosted animal experiments in facilities defined as specific pathogen-free facilities, according to FELASA guidelines. Experiments involving IL-1α KO mice were conducted at the Ben Gurion University animal facility. In both facilities mice were housed in Individually Ventilated Cages (IVC) with controlled light : dark cycle (12 : 12), room temperature (20 - 24 °C) and relative humidity (30 - 70 %). Animal caretakers, researchers and veterinarians provided mice with daily check of general health conditions. All animal experiments have been conducted in accordance with the Swiss Federal Veterinary Service guidelines and the Israel Animal Welfare Act. All mouse procedures have been previously authorized by the relevant institutional committee (Commissione Cantonale per gli Esperimenti sugli Animali) of the Cantonal Veterinary Office and by the by the Israeli Council for Animal Experimentation of the Ministry of Health, with licensing numbers TI 25/2017, TI 24/2018, TI 55/2018 and TI 30/2020. Charles River Laboratories, F. Sallusto (IRB, Bellinzona) and R. Apte (BGU, Be'er Sheva) provided, respectively, C57BL/6J, B6.129S7-Il1r1tm1Imx/J (IL-1R1KO/KO, Jackson code 003245) and IL-1α KO mice[81], which were then bred in-house. B6.129P2(Cg)-Cx3cr1tm1Litt/J (CX3CR1GFP/wt) mice were originally acquired from Jackson Laboratories (cat 005582) and bred in-house. The genotype of all mice was confirmed as previously described[82,83]. Mice in an age range of 6 - 12 weeks, showing good health conditions and no abnormal clinical signs took part in the experiments. Equal numbers of males and females were assigned to experimental groups through a statistical randomization process. Power calculation per groups size determination, performed by using R software (R: A Language and Environment for Statistical Computing, R Core Team, R Foundation for

382   Statistical Computing, Vienna, Austria), estimated a number of 10 animals per group to obtain

383   > 99 % statistical power.

Allograft model

385   10^6 cells from the syngeneic cell lines B16-F1, B16-F10 and E0771 were injected

386   subcutaneously in the right footpad in 10 µL sterile PBS. Mice were anesthetized with

387   Isoflurane (5 % for induction, 3 % for maintenance, FiO2 = 1, 1 L/min) and monitored, after

388   cells injection and anesthesia recovery, to check for absence of pain or impaired movement.

389   Mouse body weight and tumor size were measured every one or two days. Tumor volume was

390   calculated with the formula V = (length x width^2) / 2 and mice were euthanized when tumor

391   reached 250 mm^3. Euthanasia was performed by isoflurane overdose followed by cervical

392   dislocation and immediate organs collection. We excluded from experiments mice which did

393   not develop tumor (V = 0 mm^3 at day 20 p.t.i.) or which developed tumor in the popliteal fossa,

394   impeding the collection of the popliteal lymph node. In some experiments, we injected 15 µL

395   of the B16-F1 tumor cell lysate originated from 5 x 10^5 cells, sonicated at constant cycles of

396   30 seconds.

***In vivo* treatments**

398   To maximize the specific effect of treatments on LN metastases and to minimize the effect on

399   tumor engraftment and primary tumor growth, all treatments were administered when the

400   primary tumor reached a size of 40 mm^3, which corresponds to the time of arrival of the first

401   metastatic cells to the LN. Additionally, all local treatments were injected in the calf, to minimize

402   their distribution to the primary tumor. All treatments were resuspended in a maximum volume

403   of 10 µL in calcium- and magnesium-free PBS (PBS−). After injection in the subcutis, mice

404   were recovered from anesthesia and monitored for absence of any sign of pain in the foot.

405   Carrier-free recombinant mouse IL-1α (Biolegend) was locally administered at a dose of 1 µg

406   / 10 µL per day. The anti-mouse IL-1α monoclonal antibody (InVivoMAb anti-mouse IL-1α,

407   clone ALF-161, BioXCell) was administered to deplete IL-1α at a dose of 200 µg i.v. plus 60

408   µg locally, as previously reported[20]. Depletion was then maintained with a daily local injection

409   of 60 µg. STAT3 was inhibited by local injection of stattic (SelleckChem) 3.75 mg/kg every two

410   days. Stattic was reconstituted, according to manufacturer's instructions, in 5 % DMSO

411   (VWR), 40 % PEG300 (MedChem Express), 5 % Tween® 80 (Sigma-Aldrich) and 50 %

412   distilled water. For macrophages depletion, mice received locally 10 µL of clodronate- or PBS-

413   containing liposomes (Liposoma), followed by a second dose two days later.

IVIS

415   To monitor primary tumor growth and mCherry expression of fluorescent cancer cells, we used

416   the IVIS Spectrum Imaging System (Caliper LifeSciences). Mice were anesthetized with

417   isoflurane as above described to measure epifluorescence. Immediately after image

12

418   acquisition, animals were recovered from anesthesia. Images were later analyzed using Living

419   Image Software 4.2 (Caliper LifeSciences).

420   **Immunofluorescence and immunohistochemistry**

421   For mouse microscopy experiments, organs were fixed immediately after collection in 4 %

422   paraformaldehyde (Merck-Millipore) for 12 h at 4 °C, then washed in calcium- and magnesium-

423   free PBS (PBS−) and embedded in 4 % Low Gelling Temperature Agarose (Sigma-Aldrich).

424   50 µm sections were cut with a vibratome (VT1200S, Leica). Slices were stained in a blocking

425   buffer composed of TritonX100 (VWR) 0.1-0.3 %, BSA 5% (VWR) and fluorescently labelled

426   antibodies at proper concentration, all diluted in PBS supplemented with calcium and

427   magnesium (PBS+). After 72 hours of incubation at 4 °C, samples were washed in 0.05 %

428   Tween® 20 (Sigma-Aldrich), post-staining fixed with PFA 4 %, washed in PBS- and mounted

429   on glass slides. Confocal images were acquired using a Leica TCS SP5 microscope with a 20

430   x 0.7 oil objective. To quantify the rate of invasion of melanoma in each sLN region, we first

431   identified metastatic mass on the mCherry channel with an automatic Otsu threshold, after

432   noise filtering with ImageJ Despeckle plugin and size filtering for regions bigger than 30 μm^2.

433   LN regions were manually identified based on CX3CR1 and CD21/35 morphology. Next, we

434   quantified the total tumor area and the percentage of overlap of metastasis with each other

435   LN region, respectively. Sample sizes were distributed as follows: n = 21, 7 and 11 for week

436   one, two and three p.t.i., respectively. To quantify the expression of CD169^{+}, the LN regions

437   were manually identified as described above and the mean fluorescence intensity of each

438   region was later calculated. To stain IL-1α in human lymph nodes, samples were stained using

439   the BOND-III fully automated IHC/ISH stainer (Leica Biosystems) according to the

440   manufacturer's instructions. To stain STAT3 and pSTAT3, primary antibodies (mouse anti-

441   Stat3, clone 124H6, and mouse anti-Phospho-Stat3, Tyr705, clone M9C6, Cell Signaling)

442   were incubated overnight at 4°C and the MACH4 Universal HRP-Polymer Detection System

443   (Biocare Medical) was applied according to the manufacturer's protocol. 3D cell reconstruction

444   was performed using Imaris Cell Imaging Software (Oxford Instruments).

445   **Flow Cytometry**

446   LNs were collected, disrupted with tweezers, and enzymatically digested for 10 minutes at 37

447   °C. DNase I (0.28 mg/mL, VWR), dispase (1 U/mL, Corning) and collagenase P (0.5 mg/ml,

448   Roche) were resuspended in calcium- and magnesium-free PBS (PBS−). Digestion was

449   stopped using a solution of 2 mM EDTA (Sigma-Aldrich) and 2 % heat-inactivated filter-

450   sterilized fetal calf serum (Thermo Fisher Scientific) diluted in PBS− (Sigma-Aldrich). Fc

451   receptors were blocked (αCD16/32, BioLegend) followed by surface staining and analyzed by

452   flow cytometry on an LSRFortessa or FACSymphony (BD Biosciences). For IL-1α detection,

453   intracellular staining was performed with a dedicated kit (88/8824/00, eBioscience), following

13

454   the manufacturer's instructions. Data were analyzed using FlowJo software (FlowJo LLC). To

455   measure cytokines and chemokines expression in the LN, LEGENDPlex assays (Mouse

456   Proinflammatory Chemokine Panel and Mouse Inflammation Panel; BioLegend) were used.

457   Briefly, pLNs were collected and carefully disrupted in 75 µL ice-cold phosphate buffer,

458   minimizing cell rupture. The suspension was centrifuged at 100 rcf for 5 minutes and the

459   supernatant was collected. 25 µL supernatant was used for cytokines and chemokines

460   detection. Samples were analyzed by flow cytometry on an LSRFortessa or FACSymphony

461   (BD Biosciences) and data were analyzed using LEGENDPlex software (BioLegend).

462   **Antibodies**

463   The list of antibodies used to stain mouse samples includes anti-CD21/35 (CR1/CR2, clone

464   7E9, BioLegend), anti-podoplanin (clone eBio8.1.1, Invitrogen), anti-CD3 (clone 17A2,

465   BioLegend), anti-B220 (CD45R, clone RA3-6B2, BioLegend), anti-Gr-1 (clone RB6-8C5,

466   BioLegend), anti-NK1.1 (clone PK136, BioLegend), anti-MHC II (I-A/I-E, clone M5/114.15.2,

467   BioLegend), anti-CD11b (clone M1/70, BioLegend), anti-CD11c (clone N418, BioLegend),

468   anti-F4/80 (clone BM8, BioLegend), anti-CD169 (Siglec-1, clone 3D6.112), anti-IL-1R1 (clone

469   FAB7712N, R&D Systems), anti-IL-1α (clone ALF-161, BioLegend; clone REA288, Miltenyi

470   Biotec), anti-CD4 (clone RM4-5, BioLegend), anti-CD8a (clone 53-6.7, Invitrogen), anti-CD25

471   (clone PC61, BioLegend). Human samples were stained with anti-IL-1α (clone OTI2F8, Novus

472   Biologicals), and anti-CD68 antibodies (clone PG-M1, Dako).

473   **Single-cell RNA-sequencing**

474   Metastatic LN were obtained from four PBS injected mice, six tumor-bearing mice and four

475   tumor-bearing mice treated with anti-IL-1α as described above. Metastases from tumor-

476   bearing mice were microsurgically dissected using sterile micro-surgical tools. SS, IF and F

477   regions were dissected in negative controls. Later, samples were disrupted into single cell

478   suspension as described for flow cytometry, using sterile nuclease-free tools. Single cells were

479   barcoded using the 10x Chromium Single Cell platform, and cDNA libraries were prepared

480   according to the manufacturer's protocol (Single Cell 3′ v3, 10x Genomics, USA). In brief, cell

481   suspensions, reverse transcription master mix and partitioning oil were loaded on a single cell

482   chip, then run on the Chromium Controller. Reverse Transcription was performed within the

483   droplets at 53 °C for 45 minutes. cDNA was amplified for a 12 cycles total on a Biometra

484   thermocycler. cDNA size selection was performed using SpriSelect beads (Beckman Coulter,

485   USA) and a ratio of SpriSelect reagent volume to sample volume of 0.6. cDNA was analyzed

486   on an Agilent Bioanalyzer High Sensitivity DNA chip for qualitative control purposes. cDNA

487   was fragmented using the proprietary fragmentation enzyme blend for 5 minutes at 32 °C,

488   followed by end repair and A-tailing at 65 °C for 30 minutes. cDNA was double-sided size

489   selected using SpriSelect beads. Sequencing adaptors were ligated to the cDNA at 20 °C for

14

490   15 minutes. cDNA was amplified using a sample-specific index oligo as a primer, followed by

491   another round of double-sided size selection using SpriSelect beads. Final libraries were

492   analyzed on an Agilent Bioanalyzer High Sensitivity DNA chip for quality control. cDNA

493   libraries were sequenced on a NextSeq500 Illumina platform aiming for 50,000 reads per cell.

494   Base calls were converted to reads with the software Cell Ranger (10x Genomics; version 3.1)

495   **Quality control, processing, annotation, and differential gene expression analysis of**

496   **single-cell RNA-sequencing data**

497   We used the cellranger pipeline[84] to generate gene expression count matrices from the raw

498   data. For each sample, a gene-by-cell counts matrix was used to create a Seurat object using

499   Seurat[85,86]. We filtered cell barcodes with < 500 UMIs and > 5 % mitochondrial contents. Each

500   individual sample was then normalized by a factor of 10,000 and log transformed

501   (NormalizeData). The top 2000 most variable genes were then identified within each sample

502   using the FindVariableFeatures method. We then integrated the cells from all samples

503   together using FindIntegrationAnchors and IntegrateData (2000 genes). The integrated gene

504   expression matrix obtained by applying the filtering steps above was then used to perform

505   principal component analysis (RunPCA), preliminary clustering analysis, including nearest

506   neighbour graph (FindNeighbors) and unbiased clustering (FindClusters), and cell type

507   annotation. Uniform Manifold Approximation and Projection (UMAP) was then used to

508   visualise the integrated expression data. We identified gene expression markers for each

509   cluster using FindAllMarkers from Seurat with default settings, including Wilcoxon test and

510   Bonferroni p value correction[85,86]. Differential gene expression between specified clusters (or

511   subclusters) was performed using FindMarkers (Wilcoxon rank sum test) with Benjamini-

512   Hochberg false discovery rate (FDR) correction, average log fold change (logFC) and

513   detection/expression percentage rate (pct). Genes were considered (significantly) differentially

514   expressed if FDR < 0.05, logFC > 0.2 and pct > 20 % within the cells in a given group.

515   **Gene relevance analysis of single-cell RNA sequencing data**

516   To determine gene relevance across the single cell RNA sequencing data, we used a network

517   science approach. To study nodes relevance we applied Graph Theory rules[87,88] using

518   mathematical and social network analysis concepts. We restricted the analysis to protein-

519   protein interactions and to the pathways in which the gene *il1a* is involved. Relevant pathways

520   (Cytokine-cytokine receptor interaction, Necroptosis, Hematopoietic cell lineage, Type I

521   diabetes mellitus, Pertussis, Leishmaniasis, Tuberculosis and Inflammatory bowel disease)

522   and related were selected using the Kyoto Encyclopedia of Genes and Genomes[89]. Then we

523   measured the expression of these genes in our scRNA-Seq dataset and we used their

524   expression values as input of STRING[90]. The resulting graph was used for the network

525   analysis. We implemented a previously described comprehensive algorithm for evaluating

526   node influences in social networks[91]. This algorithm is based on three centrality measures:

527   eigenvector centrality[92], current flow betweenness centrality[93,94] and reachability[95].

528   Eigenvector centrality computes the centrality for a node based on the centrality of its

529   neighbors. Current-flow betweenness centrality starts from an electrical current model

530   describing the spreading pattern, to which betweenness centrality, which uses shortest paths,

531   is applied. Finally, reachability refers to the local reaching centrality of a node in a directed

532   graph as the proportion of other nodes reachable from that node. In addition single cell CMP

533   values are taken as weights of the nodes. Basing on these parameters, the algorithm ranked

534   node influences by analyzing preference relations and performing random walk. In the first

535   step a partial preference graph (PPG) is derived from the analysis of preference relation

536   between every node pair for each measure. Later, the comprehensive preference graph (CPG)

537   originated from the combination of preference relations and the three previously indicated

538   measures. Finally, a random walk was executed on CPG to determine node effect. By applying

539   this implementation to scSeq data, it was possible to obtain a list of genes related to *il1a*

540   pathways, according to their importance in our dataset.

541   **Proliferation (MTT)**

542   To evaluate tumor cells proliferation and response to treatments, B16-F1 and A375 cells were

543   seeded in a 96-well plate. Carrier-free recombinant mouse (Biolegend) or human

544   (SinoBiological) IL-1α were administered at 10 ng/mL and cells were incubated, respectively,

545   for 24 hours or 72 hours. Anti-mouse IL-1α monoclonal antibody (InVivoMAb anti-mouse IL-

546   1α, clone ALF-161, BioXCell) was administered at the indicated doses 24 hours before data

547   collection. To inhibit STAT3, stattic (SelleckChem) was administered at the indicated dosages.

548   Proliferation was assessed by MTT (Methylthiazolyldiphenyl-tetrazolium bromide) assay

549   according to the manufacturer's recommendations (Sigma). Absorbance (OD, 560 nm) was

550   measured in a microplate reader (Cytation 5, BioTek). Sensitivity to single drug treatments

551   was evaluated by IC50 (4-parameters calculation upon log-scaled doses), as previously

552   reported[96]. The beneficial effect of the combinations versus the single agents was considered

553   both as synergism according to the Chou-Talalay combination index[97], as previously

554   performed[96,98], and as potency and efficacy according to the MuSyC algorithm[99].

555   **qPCR**

556   To measure the expression of *STAT3*, *Myd88* and *Gapdh* genes, the following sets of primers

557   were designed: *STAT3* forward, 5'-CACAAATATTTTTGAGTCGGCGC-3'; *STAT3* reverse 5'-

558   AAAGCCCCCGATGAGGTAATTC-3'; *Myd88* forward, 5'-CGGCAACTAGAACAGACAGACT-

559   3'; *Myd88* reverse, 5'-GCAAACTTGGTCTGGAAGTCAC-3'; *Gapdh* forward, 5′-

560   ACATCATCCCTGCATCCACT-3′ ; *Gapdh* reverse, 5′-AGATCCACGACGGACACATT-3'. To

561   isolate RNA from cell culture, cells were disposed of in single-cell suspension in calcium- and

562 magnesium-free PBS (PBS−). RNA was isolated using an RNAeasy Mini kit (QIAGEN). Two

563 µg of cDNA were synthesized using a cDNA synthesis kit (Applied Biosystems) following the

564 manufacturer's recommendations. For the qPCR reaction, a SYBR Master Mix (Applied

565 Biosystems) was used, and samples were run on a QuantStudioTM 3 Real-Time PCR System

566 (Thermofisher). mRNA levels were expressed relative to GAPDH expression. The Pfaffl

567 method[100] was used to calculate the relative expression of the transcripts.

568 **Immunoblotting**

569 To evaluate protein expression in tumor cells, B16-F1 and A375 cells were treated using

570 carrier-free recombinant mouse (Biolegend) or human (SinoBiological) IL-1α, at 100 ng/mL.

571 To block IL-1α, anti-mouse IL-1α monoclonal antibody (InVivoMAb anti-mouse IL-1α, clone

572 ALF-161, BioXCell) was administered at the dose of 100 ng/mL. All treatments were

573 administered either for 24 hours or 72 hours. Cells were harvested and lysed by boiling

574 samples in 2x Laemmli sample buffer (BioRad), supplemented with β-mercaptoethanol

575 (Merck), for 10 minutes. Lysates (30-50 µg) were resolved according to molecular weight by

576 electrophoresis using Mini-PROTEAN TGX Precast gels 4-20 % gradient (BioRad). Next,

577 proteins were blotted onto nitrocellulose membrane (BioRad) by electric transfer and the

578 membranes were blocked in TBST (20 mM Tris-HCl [pH 7.5], 150 mM NaCl, 0.1 % Tween 20)

579 with 5 % nonfat dry milk (BioRad) for one hour at room temperature. The following primary

580 antibodies were used in TBST 5 % BSA buffer: mouse monoclonal, anti-Stat3 (clone 124H6,

581 9139, Cell Signaling Technology) and rabbit monoclonal, anti-p(Y705)Stat3 (9131, Cell

582 Signaling Technology). Mouse monoclonal anti-GAPDH (clone FF26A/F9, CNIO) was used in

583 TBST with 5 % nonfat dry milk. The secondary antibodies used were: ECL anti-mouse IgG

584 horseradish peroxidase-linked species-specific whole antibody and ECL anti-rabbit IgG

585 horseradish peroxidase-linked species-specific whole antibody (GE Healthcare). Membranes

586 were treated with Westar ηC 2.0 chemiluminescent substrate (Cyanagen) and signals were

587 detected using digital imaging with Fusion Solo (Vilber Lourmat).

588 **Statistical analyses**

589 All raw data were analyzed, processed and presented using GraphPad Prism 8.2.1 (Graphpad

590 Software, La Jolla, USA). First, we applied the Shapiro-Wilk normality test to analyze the

591 distribution of data. Then we compared means among groups using One-Way ANOVA or

592 Unpaired t test for data with normal distribution, and the non-parametric Kruskal-Wallis or

593 Mann-Whitney test for groups which did not present a normal distribution. In all statistical tests

594 P value is indicated as * when <0.05, ** when <0.005, *** when <0.0005, **** when < 0.0001.

18

REFERENCES

1. Carr S, Smith C, Wernberg J. Epidemiology and Risk Factors of Melanoma. *Surg Clin North Am*. 2020;100(1):1-12. doi:10.1016/j.suc.2019.09.005

2. Karlsson MC, Gonzalez SF, Welin J, Fuxe J. Epithelial-mesenchymal transition in cancer metastasis through the lymphatic system. *Mol Oncol*. 2017;11(7):781-791. doi:10.1002/1878-0261.12092

3. Damsky WE, Rosenbaum LE, Bosenberg M. Decoding melanoma metastasis. *Cancers (Basel)*. 2011;3(1):126-163. doi:10.3390/cancers3010126

4. Ulmer A, Dietz K, Hodak I, et al. Quantitative Measurement of Melanoma Spread in Sentinel Lymph Nodes and Survival. *PLoS Med*. 2014;11(2):e1001604. doi:10.1371/journal.pmed.1001604

5. JE G, RA S, KR H, et al. Melanoma staging: Evidence-based changes in the American Joint Committee on Cancer eighth edition cancer staging manual. *CA Cancer J Clin*. 2017;67(6):472-492. doi:10.3322/CAAC.21409

6. Wiley HE, Gonzalez EB, Maki W, Wu MT, Hwang ST. Expression of CC chemokine receptor-7 and regional lymph node metastasis of B16 murine melanoma. *J Natl Cancer Inst*. 2001;93(21):1638-1643. doi:10.1093/jnci/93.21.1638

7. A B-B. Organ selectivity in metastasis: regulation by chemokines and their receptors. *Clin Exp Metastasis*. 2008;25(4):345-356. doi:10.1007/S10585-007-9097-3

8. Das S, Sarrou E, Podgrabinska S, et al. Tumor cell entry into the lymph node is controlled by CCL1 chemokine expressed by lymph node lymphatic sinuses. *J Exp Med*. 2013;210(8):1509-1528. doi:10.1084/jem.20111627

9. Singh R, Choi BK. Siglec1-expressing subcapsular sinus macrophages provide soil for melanoma lymph node metastasis. *Elife*. 2019;8. doi:10.7554/eLife.48916

10. Kretschmer L, Mitteldorf C, Hellriegel S, et al. The sentinel node invasion level (SNIL) as a prognostic parameter in melanoma. *Mod Pathol 2021*. Published online June 15, 2021:1-11. doi:10.1038/s41379-021-00835-5

11. Brown M, Assen FP, Leithner A, et al. Lymph node blood vessels provide exit routes for metastatic tumor cell dissemination in mice. *Science (80-)*. 2018;359(6382):1408-1411. doi:10.1126/science.aal3662

12. Pereira ER, Kedrin D, Seano G, et al. Lymph node metastases can invade local blood vessels, exit the node, and colonize distant organs in mice. *Science (80-)*. 2018;359(6382):1403-1407. doi:10.1126/science.aal3622

638   13.   Ubellacker JM, Tasdogan A, Ramesh V, et al. Lymph protects metastasizing
639   melanoma cells from ferroptosis. *Nature*. 2020;585(7823):113-118.
640   doi:10.1038/s41586-020-2623-z

641   14.   Gray EE, Cyster JG. Lymph node macrophages. *J Innate Immun*. 2012;4(5-6):424-
642   436. doi:10.1159/000337007

643   15.   Kuka M, Iannacone M. The role of lymph node sinus macrophages in host defense.
644   *Ann N Y Acad Sci*. 2014;1319(1):38-46. doi:10.1111/NYAS.12387

645   16.   YR C, FD B. B cells acquire particulate antigen in a macrophage-rich area at the
646   boundary between the follicle and the subcapsular sinus of the lymph node. *Immunity*.
647   2007;27(1):160-171. doi:10.1016/J.IMMUNI.2007.06.007

648   17.   M I, EA M, E T, et al. Subcapsular sinus macrophages prevent CNS invasion on
649   peripheral infection with a neurotropic virus. *Nature*. 2010;465(7301):1079-1083.
650   doi:10.1038/NATURE09118

651   18.   SF G, V L-K, MP K, et al. Capture of influenza by medullary dendritic cells via SIGN-
652   R1 is essential for humoral immunity in draining lymph nodes. *Nat Immunol*.
653   2010;11(5):427-434. doi:10.1038/NI.1856

654   19.   M G, A C, B M, et al. Host response. Inflammation-induced disruption of SCS
655   macrophages impairs B cell responses to secondary infection. *Science*.
656   2015;347(6222):667-672. doi:10.1126/SCIENCE.AAA1300

657   20.   Chatziandreou N, Farsakoglu Y, Palomino-Segura M, et al. Macrophage Death
658   following Influenza Vaccination Initiates the Inflammatory Response that Promotes
659   Dendritic Cell Function in the Draining Lymph Node. *Cell Rep*. 2017;18(10):2427-
660   2440. doi:10.1016/j.celrep.2017.02.026

661   21.   Asano K, Nabeyama A, Miyake Y, et al. CD169-Positive Macrophages Dominate
662   Antitumor Immunity by Crosspresenting Dead Cell-Associated Antigens. *Immunity*.
663   2011;34(1):85-95. doi:10.1016/j.immuni.2010.12.011

664   22.   Kumamoto K, Tasaki T, Ohnishi K, et al. CD169 Expression on Lymph Node
665   Macrophages Predicts in Patients With Gastric Cancer. *Front Oncol*. 2021;11:824.
666   doi:10.3389/FONC.2021.636751

667   23.   Moalli F, Proulx ST, Schwendener R, Detmar M, Schlapbach C, Stein J V. Intravital
668   and whole-organ imaging reveals capture of melanoma-derived antigen by lymph
669   node subcapsular macrophages leading to widespread deposition on follicular
670   dendritic cells. *Front Immunol*. 2015;6(MAR). doi:10.3389/fimmu.2015.00114

671   24.   Pucci F, Garris C, Lai CP, et al. SCS macrophages suppress melanoma by restricting
672   tumor-derived vesicle-B cell interactions. Published online 2016.

673   doi:10.1126/science.aaf1328

674   25.   Louie DAP, Liao S. Lymph Node Subcapsular Sinus Macrophages as the Frontline of

675   Lymphatic Immune Defense. *Front Immunol*. 2019;10(FEB):347.

676   doi:10.3389/FIMMU.2019.00347

677   26.   Björk Gunnarsdottir F, Auoja N, Bendahl P-O, Rydén L, Fernö M, Leandersson K. Co-

678   localization of CD169+ macrophages and cancer cells in lymph node metastases of

679   breast cancer patients is linked to improved prognosis and PDL1 expression.

680   *Oncoimmunology*. 2020;9(1):1848067. doi:10.1080/2162402X.2020.1848067

681   27.   Tacconi C, Commerford CD, Dieterich LC, et al. CD169+ lymph node macrophages

682   have protective functions in mouse breast cancer metastasis. *Cell Rep*.

683   2021;35(2):108993. doi:10.1016/j.celrep.2021.108993

684   28.   Balkwill F, Charles KA, Mantovani A. Smoldering and polarized inflammation in the

685   initiation and promotion of malignant disease. *Cancer Cell*. 2005;7(3):211-217.

686   doi:10.1016/j.ccr.2005.02.013

687   29.   Mantovani A, Allavena P, Sica A, Balkwill F. Cancer-related inflammation. *Nature*.

688   2008;454(7203):436-444. doi:10.1038/nature07205

689   30.   Cassetta L, Fragkogianni S, Sims AH, Coussens LM, Smith HO, Pollard

690   Correspondence JW. Human Tumor-Associated Macrophage and Monocyte

691   Transcriptional Landscapes Reveal Cancer-Specific Reprogramming, Biomarkers,

692   and Therapeutic Targets. Published online 2019. doi:10.1016/j.ccell.2019.02.009

693   31.   Birmingham KG, O'Melia MJ, Bordy S, et al. Lymph Node Subcapsular Sinus

694   Microenvironment-On-A-Chip Modeling Shear Flow Relevant to Lymphatic Metastasis

695   and Immune Cell Homing. *iScience*. 2020;23(11):101751.

696   doi:10.1016/J.ISCI.2020.101751

697   32.   Balkwill F, Mantovani A. Inflammation and cancer: Back to Virchow? *Lancet*.

698   2001;357(9255):539-545. doi:10.1016/S0140-6736(00)04046-0

699   33.   Spranger S, Luke JJ, Bao R, et al. Density of immunogenic antigens does not explain

700   the presence or absence of the T-cell-inflamed tumor microenvironment in melanoma.

701   *Proc Natl Acad Sci U S A*. 2016;113(48):E7759-E7768.

702   doi:10.1073/pnas.1609376113

703   34.   Trujillo JA, Sweis RF, Bao R, Luke JJ. T cell–inflamed versus Non-T cell–inflamed

704   tumors: a conceptual framework for cancer immunotherapy drug development and

705   combination therapy selection. *Cancer Immunol Res*. 2018;6(9):990-1000.

706   doi:10.1158/2326-6066.CIR-18-0277

707   35.   Ochoa de Olza M, Navarro Rodrigo B, Zimmermann S, Coukos G. Turning up the

708 heat on non-immunoreactive tumours: opportunities for clinical development. *Lancet*
709 *Oncol*. 2020;21(9):e419-e430. doi:10.1016/S1470-2045(20)30234-5

710 36. Voronov E, Dotan S, Krelin Y, et al. Unique versus redundant functions of IL-1α and
711 IL-1β in the tumor microenvironment. *Front Immunol*. 2013;4(JUL):177.
712 doi:10.3389/fimmu.2013.00177

713 37. RN A, S D, M E, et al. The involvement of IL-1 in tumorigenesis, tumor invasiveness,
714 metastasis and tumor-host interactions. *Cancer Metastasis Rev*. 2006;25(3):387-408.
715 doi:10.1007/S10555-006-9004-4

716 38. Kaplanov I, Carmi Y, Kornetsky R, et al. Blocking IL-1β reverses the
717 immunosuppression in mouse breast cancer and synergizes with anti–PD-1 for tumor
718 abrogation. *Proc Natl Acad Sci U S A*. 2019;116(4):1361-1369.
719 doi:10.1073/pnas.1812266115

720 39. Mantovani A, Dinarello CA, Molgora M, Garlanda C. Interleukin-1 and Related
721 Cytokines in the Regulation of Inflammation and Immunity. *Immunity*. 2019;50(4):778-
722 795. doi:10.1016/j.immuni.2019.03.012

723 40. Lust JA, Lacy MQ, Zeldenrust SR, et al. Induction of a chronic disease state in
724 patients with smoldering or indolent multiple myeloma by targeting interleukin 1β-
725 induced interleukin 6 production and the myeloma proliferative component. *Mayo Clin*
726 *Proc*. 2009;84(2):114-122. doi:10.4065/84.2.114

727 41. Hong DS, Hui D, Bruera E, et al. MABp1, a first-in-class true human antibody
728 targeting interleukin-1α in refractory cancers: An open-label, phase 1 dose-escalation
729 and expansion study. *Lancet Oncol*. 2014;15(6):656-666. doi:10.1016/S1470-
730 2045(14)70155-X

731 42. Hong DS, Janku F, Naing A, et al. Xilonix, a novel true human antibody targeting the
732 inflammatory cytokine interleukin-1 alpha, in non-small cell lung cancer. *Invest New*
733 *Drugs*. 2015;33(3):621-631. doi:10.1007/s10637-015-0226-6

734 43. Lust JA, Lacy MQ, Zeldenrust SR, et al. Reduction in C-reactive protein indicates
735 successful targeting of the IL-1/IL-6 axis resulting in improved survival in early stage
736 multiple myeloma. *Am J Hematol*. 2016;91(6):571-574. doi:10.1002/ajh.24352

737 44. Hickish T, Andre T, Wyrwicz L, et al. MABp1 as a novel antibody treatment for
738 advanced colorectal cancer: a randomised, double-blind, placebo-controlled, phase 3
739 study. *Lancet Oncol*. 2017;18(2):192-201. doi:10.1016/S1470-2045(17)30006-2

740 45. Janssen LME, Ramsay EE, Logsdon CD, Overwijk WW. The immune system in
741 cancer metastasis: Friend or foe? *J Immunother Cancer*. 2017;5(1):79.
742 doi:10.1186/s40425-017-0283-9

743   46.   Garner H, de Visser KE. Immune crosstalk in cancer progression and metastatic
744   spread: a complex conversation. *Nat Rev Immunol*. 2020;20(8):483-497.
745   doi:10.1038/s41577-019-0271-z

746   47.   Hiam-Galvez KJ, Allen BM, Spitzer MH. Systemic immunity in cancer. *Nat Rev
747   Cancer*. Published online April 9, 2021:1-15. doi:10.1038/s41568-021-00347-z

748   48.   Edwards SC, Hoevenaar WHM, Coffelt SB. Emerging immunotherapies for
749   metastasis. *Br J Cancer*. 2021;124(1):37-48. doi:10.1038/s41416-020-01160-5

750   49.   Ralli M, Botticelli A, Visconti IC, et al. Immunotherapy in the Treatment of Metastatic
751   Melanoma: Current Knowledge and Future Directions. *J Immunol Res*. 2020;2020.
752   doi:10.1155/2020/9235638

753   50.   Michielin O, Atkins MB, Koon HB, Dummer R, Ascierto PA. Evolving impact of long-
754   Term survival results on metastatic melanoma treatment. *J Immunother Cancer*.
755   2020;8(2):948. doi:10.1136/jitc-2020-000948

756   51.   Lee C kun, Jeong S hwan, Jang C, et al. Tumor metastasis to lymph nodes requires
757   YAP-dependent metabolic adaptation. *Science (80-)*. 2019;363(6427):644-649.
758   doi:10.1126/science.aav0173

759   52.   Pizzagalli DU, Latino I, Pulfer A, et al. Characterization of the Dynamic Behavior of
760   Neutrophils Following Influenza Vaccination. *Front Immunol*. 2019;10.
761   doi:10.3389/fimmu.2019.02621

762   53.   Fu X-Q, Liu B, Wang Y-P, et al. Activation of STAT3 is a key event in TLR4 signaling-
763   mediated melanoma progression. *Cell Death Dis 2020 114*. 2020;11(4):1-15.
764   doi:10.1038/s41419-020-2440-1

765   54.   A S, R S, O E, et al. STAT3 promotes melanoma metastasis by CEBP-induced
766   repression of the MITF pathway. *Oncogene*. 2021;40(6):1091-1105.
767   doi:10.1038/S41388-020-01584-6

768   55.   Malvehy J, Puig S. Expression of Stat3 and Src proteins in mucosal, cutaneous, and
769   metastatic melanoma. *J Am Acad Dermatol*. 2005;52(3):P144.
770   doi:10.1016/J.JAAD.2004.10.584

771   56.   Lin W-H, Chang Y-W, Hong M-X, et al. STAT3 phosphorylation at Ser727 and Tyr705
772   differentially regulates the EMT–MET switch and cancer metastasis. *Oncogene 2020
773   404*. 2020;40(4):791-805. doi:10.1038/s41388-020-01566-8

774   57.   Zerdes I, Wallerius M, Sifakis EG, et al. STAT3 Activity Promotes Programmed-Death
775   Ligand 1 Expression and Suppresses Immune Responses in Breast Cancer. *Cancers
776   (Basel)*. 2019;11(10). doi:10.3390/CANCERS11101479

777   58.   Zou S, Tong Q, Liu B, Huang W, Tian Y, Fu X. Targeting STAT3 in Cancer

778   Immunotherapy. *Mol Cancer 2020 191*. 2020;19(1):1-19. doi:10.1186/S12943-020-
779   01258-7

780   59.   Hoeller C. The future of combination therapies in advanced melanoma. *memo - Mag*
781   *Eur Med Oncol 2020 133*. 2020;13(3):309-313. doi:10.1007/S12254-020-00640-X

782   60.   Yu C, Liu X, Yang J, et al. Combination of Immunotherapy With Targeted Therapy:
783   Theory and Practice in Metastatic Melanoma. *Front Immunol*. 2019;0(MAY):990.
784   doi:10.3389/FIMMU.2019.00990

785   61.   Berraondo P, Sanmamed MF, Ochoa MC, et al. Cytokines in clinical cancer
786   immunotherapy. *Br J Cancer 2018 1201*. 2018;120(1):6-15. doi:10.1038/s41416-018-
787   0328-y

788   62.   Johnson DE, O'Keefe RA, Grandis JR. Targeting the IL-6/JAK/STAT3 signalling axis
789   in cancer. *Nat Rev Clin Oncol 2018 154*. 2018;15(4):234-248.
790   doi:10.1038/nrclinonc.2018.8

791   63.   Lippitz BE, Harris RA. Cytokine patterns in cancer patients: A review of the correlation
792   between interleukin 6 and prognosis. *Oncoimmunology*. 2016;5(5).
793   doi:10.1080/2162402X.2015.1093722

794   64.   Kurzrock R, Hickish T, Wyrwicz L, et al. Interleukin-1 receptor antagonist levels
795   predict favorable outcome after bermekimab, a first-in-class true human interleukin-1α
796   antibody, in a phase III randomized study of advanced colorectal cancer.
797   *Oncoimmunology*. 2019;8(3). doi:10.1080/2162402X.2018.1551651

798   65.   Kauffmann-Guerrero D, Kahnert K, Kiefl R, et al. Systemic inflammation and pro-
799   inflammatory cytokine profile predict response to checkpoint inhibitor treatment in
800   NSCLC: a prospective study. *Sci Reports 2021 111*. 2021;11(1):1-10.
801   doi:10.1038/s41598-021-90397-y

802   66.   Wang M, Zhai X, Li J, et al. The Role of Cytokines in Predicting the Response and
803   Adverse Events Related to Immune Checkpoint Inhibitors. *Front Immunol*.
804   2021;0:2894. doi:10.3389/FIMMU.2021.670391

805   67.   Perrichet A, Ghiringhelli F, Rébé C. Understanding Inflammasomes and PD-1/PD-L1
806   Crosstalk to Improve Cancer Treatment Efficiency. *Cancers (Basel)*. 2020;12(12):1-
807   19. doi:10.3390/CANCERS12123550

808   68.   Ashizawa T, Iizuka A, Maeda C, et al. Impact of combination therapy with anti-PD-1
809   blockade and a STAT3 inhibitor on the tumor-infiltrating lymphocyte status. *Immunol*
810   *Lett*. 2019;216:43-50. doi:10.1016/J.IMLET.2019.10.003

811   69.   MW M, RC M, M Q, et al. Immune response in melanoma: an in-depth analysis of the
812   primary tumor and corresponding sentinel lymph node. *Mod Pathol*. 2012;25(7):1000-

813   1010. doi:10.1038/MODPATHOL.2012.43

814   70.   Chitty JL, Filipe EC, Lucas MC, Herrmann D, Cox TR, Timpson P. Recent advances

815   in understanding the complexities of metastasis. *F1000Research*. 2018;7.

816   doi:10.12688/F1000RESEARCH.15064.2

817   71.   Zhou H, Lei P, Padera TP. Progression of Metastasis through Lymphatic System.

818   *Cells 2021, Vol 10, Page 627*. 2021;10(3):627. doi:10.3390/CELLS10030627

819   72.   Hu J, Xu J, Li M, et al. Targeting Lymph Node Sinus Macrophages to Inhibit Lymph

820   Node Metastasis. *Mol Ther Nucleic Acid*. 2019;16:650-662.

821   doi:10.1016/j.omtn.2019.04.016

822   73.   Mantovani A, Marchesi F, Jaillon S, Garlanda C, Allavena P. Tumor-associated

823   myeloid cells: diversity and therapeutic targeting. *Cell Mol Immunol*. 2021;18(3):566-

824   578. doi:10.1038/s41423-020-00613-4

825   74.   Tacconi C, Commerford CD, Dieterich LC, et al. CD169+ lymph node macrophages

826   have protective functions in mouse breast cancer metastasis. *Cell Rep*.

827   2021;35(2):108993. doi:10.1016/j.celrep.2021.108993

828   75.   Cassetta L, Pollard JW. Repolarizing macrophages improves breast cancer therapy.

829   *Cell Res 2017 278*. 2017;27(8):963-964. doi:10.1038/cr.2017.63

830   76.   Crecente-Campo J, Virgilio T, Morone D, et al. Design of polymeric nanocapsules to

831   improve their lympho-targeting capacity. *Nanomedicine*. 2019;14(23).

832   doi:10.2217/nnm-2019-0206

833   77.   Schudel A, Francis DM, Thomas SN. Material design for lymph node drug delivery.

834   *Nat Rev Mater*. 2019;4(6):415. doi:10.1038/S41578-019-0110-7

835   78.   Grabowska J, Lopez-Venegas MA, Affandi AJ, den Haan JMM. CD169+

836   Macrophages Capture and Dendritic Cells Instruct: The Interplay of the Gatekeeper

837   and the General of the Immune System. *Front Immunol*. 2018;9(OCT):2472.

838   doi:10.3389/FIMMU.2018.02472

839   79.   Rider P, Kaplanov I, Romzova M, et al. The transcription of the alarmin cytokine

840   interleukin-1 alpha is controlled by hypoxia inducible factors 1 and 2 alpha in hypoxic

841   cells. *Front Immunol*. 2012;3(SEP). doi:10.3389/FIMMU.2012.00290

842   80.   Kurzrock R, Hickish T, Wyrwicz L, et al. Interleukin-1 receptor antagonist levels

843   predict favorable outcome after bermekimab, a first-in-class true human interleukin-1α

844   antibody, in a phase III randomized study of advanced colorectal cancer.

845   *Oncoimmunology*. 2019;8(3). doi:10.1080/2162402X.2018.1551651

846   81.   Horai R, Asano M, Sudo K, et al. Production of mice deficient in genes for interleukin

847   (IL)-1α, IL-1β, IL-1α/β, and IL-1 receptor antagonist shows that IL-1β is crucial in

848   turpentine-induced fever development and glucocorticoid secretion. *J Exp Med*.
849   1998;187(9):1463-1475. doi:10.1084/jem.187.9.1463

850 82.   Glaccum MB, Stocking KL, Charrier K, et al. Phenotypic and functional
851   characterization of mice that lack the type I receptor for IL-1. *J Immunol*.
852   1997;159(7):3364-3371. http://www.ncbi.nlm.nih.gov/pubmed/9317135

853 83.   Jung S, Aliberti J, Graemmel P, et al. Analysis of Fractalkine Receptor CX3CR1
854   Function by Targeted Deletion and Green Fluorescent Protein Reporter Gene
855   Insertion. *Mol Cell Biol*. 2000;20(11):4106-4114. doi:10.1128/mcb.20.11.4106-
856   4114.2000

857 84.   Zheng GXY, Terry JM, Belgrader P, et al. Massively parallel digital transcriptional
858   profiling of single cells. *Nat Commun*. 2017;8(1):1-12. doi:10.1038/ncomms14049

859 85.   Butler A, Hoffman P, Smibert P, Papalexi E, Satija R. Integrating single-cell
860   transcriptomic data across different conditions, technologies, and species. *Nat
861   Biotechnol*. 2018;36(5):411-420. doi:10.1038/nbt.4096

862 86.   Stuart T, Butler A, Hoffman P, et al. Comprehensive Integration of Single-Cell Data.
863   *Cell*. 2019;177(7):1888-1902.e21. doi:10.1016/j.cell.2019.05.031

864 87.   Catlin PA, Chartrand G. Introductory Graph Theory. *Am Math Mon*. 1987;94(5):483.
865   doi:10.2307/2322751

866 88.   Meyer B. *Self-Organizing Graphs-A Neural Network Perspective of Graph Layout*.

867 89.   Kanehisa M, Furumichi M, Tanabe M, Sato Y, Morishima K. KEGG: New perspectives
868   on genomes, pathways, diseases and drugs. *Nucleic Acids Res*. 2017;45(D1):D353-
869   D361. doi:10.1093/nar/gkw1092

870 90.   Szklarczyk D, Gable AL, Lyon D, et al. STRING v11: Protein-protein association
871   networks with increased coverage, supporting functional discovery in genome-wide
872   experimental datasets. *Nucleic Acids Res*. 2019;47(D1):D607-D613.
873   doi:10.1093/nar/gky1131

874 91.   Mao C, Xiao W. A comprehensive algorithm for evaluating node influences in social
875   networks based on preference analysis and random walk. *Complexity*. 2018;2018.
876   doi:10.1155/2018/1528341

877 92.   Bihari A, Pandia MK. Eigenvector centrality and its application in research
878   professionals' relationship network. In: *2015 1st International Conference on Futuristic
879   Trends in Computational Analysis and Knowledge Management, ABLAZE 2015*.
880   Institute of Electrical and Electronics Engineers Inc.; 2015:510-514.
881   doi:10.1109/ABLAZE.2015.7154915

882 93.   Brandes U, Fleischer D. Centrality measures based on current flow. In: *Lecture Notes*

883   *in Computer Science*. Vol 3404. Springer Verlag; 2005:533-544. doi:10.1007/978-3-
884   540-31856-9_44

885   94. Newman MEJ. A measure of betweenness centrality based on random walks. *Soc*
886   *Networks*. 2003;27(1):39-54. Accessed April 9, 2021. http://arxiv.org/abs/cond-
887   mat/0309045

888   95. Mones E. Hierarchy in directed random networks. *Phys Rev E - Stat Nonlinear, Soft*
889   *Matter Phys*. 2013;87(2):022817. doi:10.1103/PhysRevE.87.022817

890   96. C T, E G, AJ A, et al. PQR309 Is a Novel Dual PI3K/mTOR Inhibitor with Preclinical
891   Antitumor Activity in Lymphomas as a Single Agent and in Combination Therapy. *Clin*
892   *Cancer Res*. 2018;24(1):120-129. doi:10.1158/1078-0432.CCR-17-1041

893   97. TC C. Drug combination studies and their synergy quantification using the Chou-
894   Talalay method. *Cancer Res*. 2010;70(2):440-446. doi:10.1158/0008-5472.CAN-09-
895   1947

896   98. Gaudio E, Tarantelli C, Spriano F, et al. Targeting CD205 with the antibody drug
897   conjugate MEN1309/OBT076 is an active new therapeutic strategy in lymphoma
898   models. *Haematologica*. 2020;105(11):2584-2591.
899   doi:10.3324/HAEMATOL.2019.227215

900   99. Meyer CT, Wooten DJ, Paudel BB, et al. Quantifying Drug Combination Synergy
901   along Potency and Efficacy Axes. *Cell Syst*. 2019;8(2):97-108.e16.
902   doi:10.1016/J.CELS.2019.01.003

903   100. Pfaffl MW. A new mathematical model for relative quantification in real-time RT-PCR.
904   *Nucleic Acids Res*. 2001;29(9). doi:10.1093/nar/29.9.e45

905

FIGURES LEGEND

Figure 1. Mouse melanoma metastases growth in the sentinel LN. (A) FACS plot showing fluorescent expression of the mCherry transduced B16-F1 melanoma cells. (B) Schematic representation of the tumor model, including primary tumor engraftment (left) and migration of cells to the sLN (right). (C) Representative images and (D) quantification of IVIS time-course showing increasing primary tumor fluorescence (red). (E, left) Primary tumor (red arrow), draining sentinel LN (white circle) and (E, right) comparison between metastatic and healthy LN at week three p.t.i.. (F) Time-course of metastatic cell invasion of the sLN quantified by FACS. (G) Confocal micrograph of sLN at week one, two and three p.t.i., showing the position of B16 melanoma (red) with respect to CD21/35$^+$ (blue) follicular dendritic cells and CX3CR1$^+$ (green) myeloid cells. SS, IF, F, T and M stand for subcapsular sinus, inter-follicular, follicular, T cells and medullary areas, respectively. (H) Quantification of total metastatic area in the sLN, measured by confocal microscopy. (I) Quantification of tumor cells in the different compartments of the LN at week two and three p.t.i.. (J) Metastatic ratio, defined as the number of mice with metastases in the target organ divided by the total number of implanted mice, at week three p.t.i.. iLN stands for inguinal LN.

Figure 2. Pro-tumoral release of IL-1α in the metastatic LN

(A) Progressive increase in the size of the sLN correlated with the increase in the total number of immune cells, measured by flow cytometry. (B) Quantification of inflammatory cytokines in the supernatant of metastatic (red) and non-metastatic (white) LN. (C) Time course kinetics showing IL-1α release in the sLN during the first three weeks p.t.i.. (D) Quantification of IL-1α in the sLN at three weeks p.t.i. of different cancer models, including breast cancer (E0771) and the melanoma B16-F10. (E) Flow cytometric quantification of LN metastatic cells in animals treated with IL-1α depleting antibody or recombinant IL-1α in comparison to B16-F1 untreated group and PBS injected. (F) LN metastatic ratio in mice untreated or treated with anti-IL-1α antibody or recombinant IL-1α at week three p.t.i.. (G) Metastatic cells in the sLN of wild type and IL-1α KO mice three weeks p.t.i..

Figure 3. SSM are the main source of IL-1α. (A) UMAP plot of cell populations, identified by scSeq, in the metastasized sLN three weeks p.t.i.. (B) Percentage of cells expressing il1a and (C) average il1a expression in the cells of the sLN three weeks p.t.i., measured by scSeq. (D) IL-1α quantification in metastasized sLN supernatant of mice depleted for macrophages by clodronate liposome (CLL) injection in comparison to untreated metastasized and non-metastasized LN. (E) Flow cytometric histograms showing presence, three weeks p.t.i., of IL-1α$^+$ (red) and IL-1α$^-$ negative (gray) SSM. (F) Flow cytometric quantification of the number of IL-1α$^+$ cells among the three major subtypes of macrophages in the sLN three weeks p.t.i. in comparison to negative controls. SSM, MCM and MM stand for Subcapsular Sinus Macrophages (CD169$^+$ F4/80$^-$), Medullary Cord Macrophages (CD169$^-$ F4/80$^+$) and Medullary Macrophages (CD169$^+$ F4/80$^+$), respectively. (G) Confocal micrograph showing the whole sLN (left) and magnifications of the metastatic region (center and right) indicating IL-1α and

28

945   *tumor vesicles in CX3CR1$^+$ CD169$^+$ macrophages. Colors indicate CX3XR1$^+$ cells (green), mCherry$^+$*

946   *melanoma (red), CD169$^+$ macrophages (cyan) and IL-1α (white). (H) Flow cytometric quantification*

947   *indicating the number of each subtype of tumor$^+$ macrophages. (I) Confocal representative images of*

948   *CD169$^+$ macrophages distribution in the sLN three weeks p.t.i. in comparison to negative controls. (J)*

949   *Quantification of CD169 fluorescence in the main regions of the LN three weeks p.t.i., indicating*

950   *disruption of CD169 layer (white arrows) in the SS overlying the metastatic area (SS^{MET}).*

951

952   ***Figure 4. Direct effect of pro-tumoral IL-1α on metastatic cells.*** *(A) Flow cytometry quantification of*

953   *mean fluorescence intensity (MFI) indicating IL-1R1 expression in the sLN cell populations. (B) Flow*

954   *cytometric quantification of metastatic cells and (C) metastatic ratio in wild type and IL-1R1 knock-out*

955   *mice, three weeks p.t.i.. (D) Proliferation assay (MTT) of B16-F1 treated with recombinant IL-1α for 24*

956   *h in comparison to untreated cells. (E) Proliferation assay (MTT) of human melanoma A375 treated with*

957   *human recombinant IL-1α for 72 h, in comparison to untreated cells. (F) qPCR quantification of the*

958   *Myd88 gene in B16-F1 stimulated with recombinant IL-1α in comparison to unstimulated.*

959

960   ***Figure 5. IL-1α induces STAT3 expression and phosphorylation in tumor.*** *(A) STRING graph*

961   *representing the most influential genes obtained by node influence analysis of il1a enriched pathways*

962   *in scSeq data of the metastatic area of the sLN. The influence of each node is expressed in a*

963   *colorimetric scale. (B) Bar plot showing node influence of the ten most influential genes in il1a*

964   *pathways three weeks p.t.i.. STAT3 is highlighted (red). (C) Bar plot indicating differential expression*

965   *(DE) of the ten most influential nodes in tumor following IL-1α block in comparison to untreated mice.*

966   *STAT3 is highlighted (red). (D) Average STAT3 expression in each cell population of the metastatic*

967   *sLN. (E) qPCR quantification of STAT3 expression in B16-F1 following recombinant IL-1α*

968   *administration. Quantification of (F) STAT3 and (G) pSTAT3, measured by immunoblot, in B16-F1*

969   *after IL-1α treatment. Immunoblot quantifications of (H) STAT3 and (I) pSTAT3 in human melanoma*

970   *A375 following exposure to IL-1α. (J) Flow cytometric quantification of metastatic cells in mouse sLN*

971   *of mice treated with anti-IL-1α antibody, the STAT3 inhibitor stattic or their combination, in comparison*

972   *to untreated. (K) Proliferation of mouse melanoma upon combination therapy with anti-IL-1α stattic at*

973   *different concentrations, measured by MTT assay.*

29

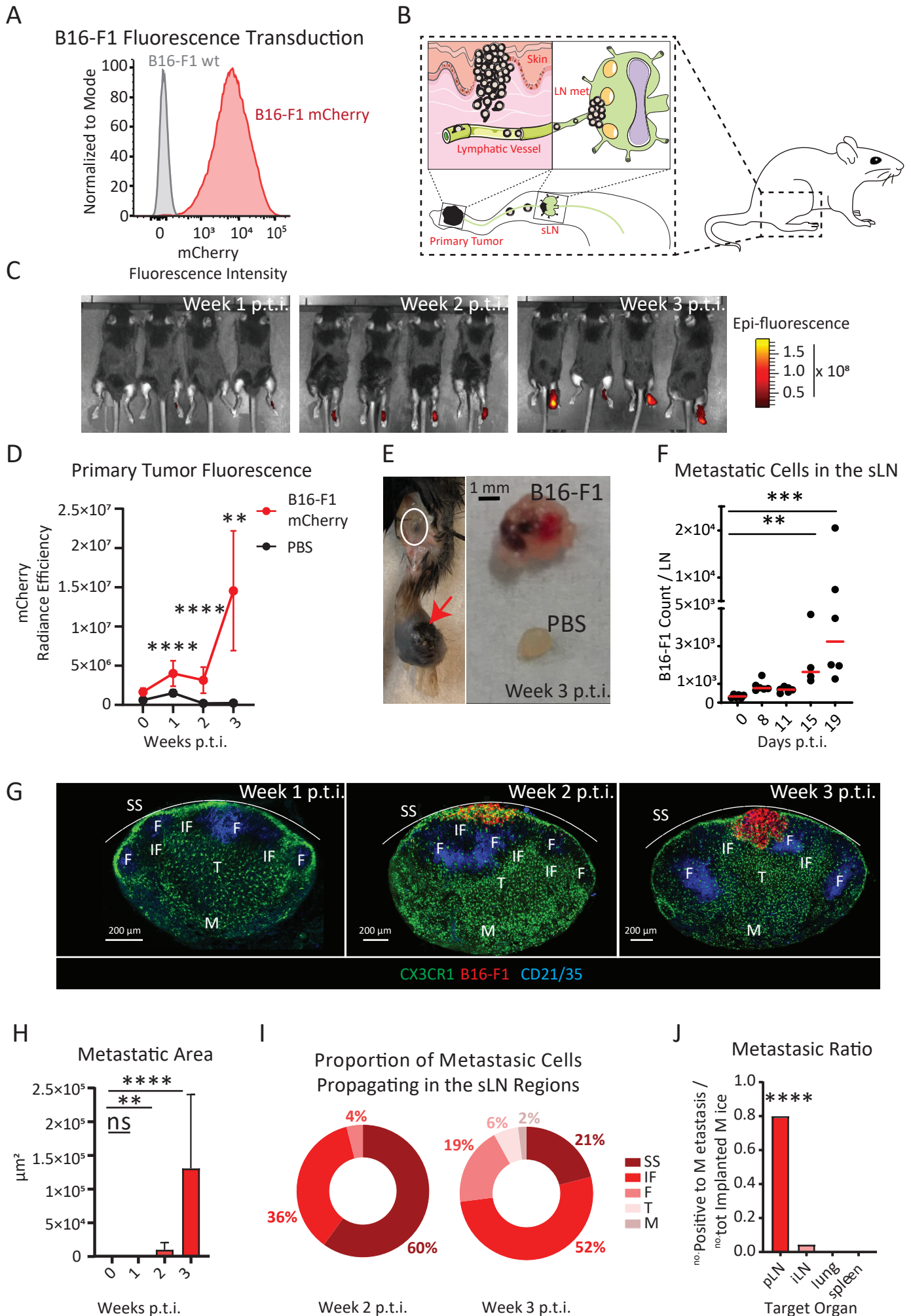**Figure 1.** Mouse melanoma metastases growth in the sentinel LN.

CX3CR1 B16-F1 CD21/35

Figure 2. Pro-tumoral release of IL-1α in the metastatic LN
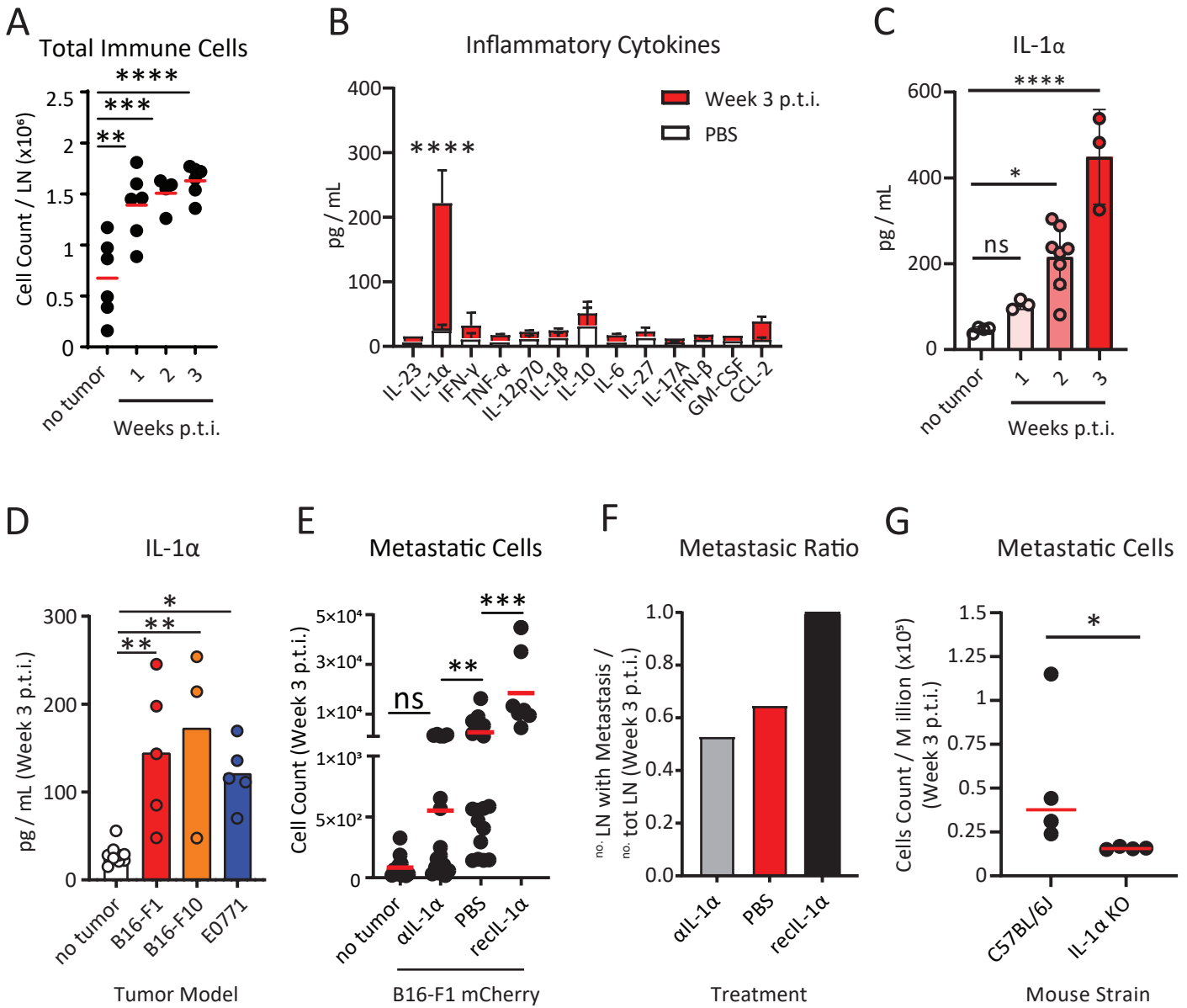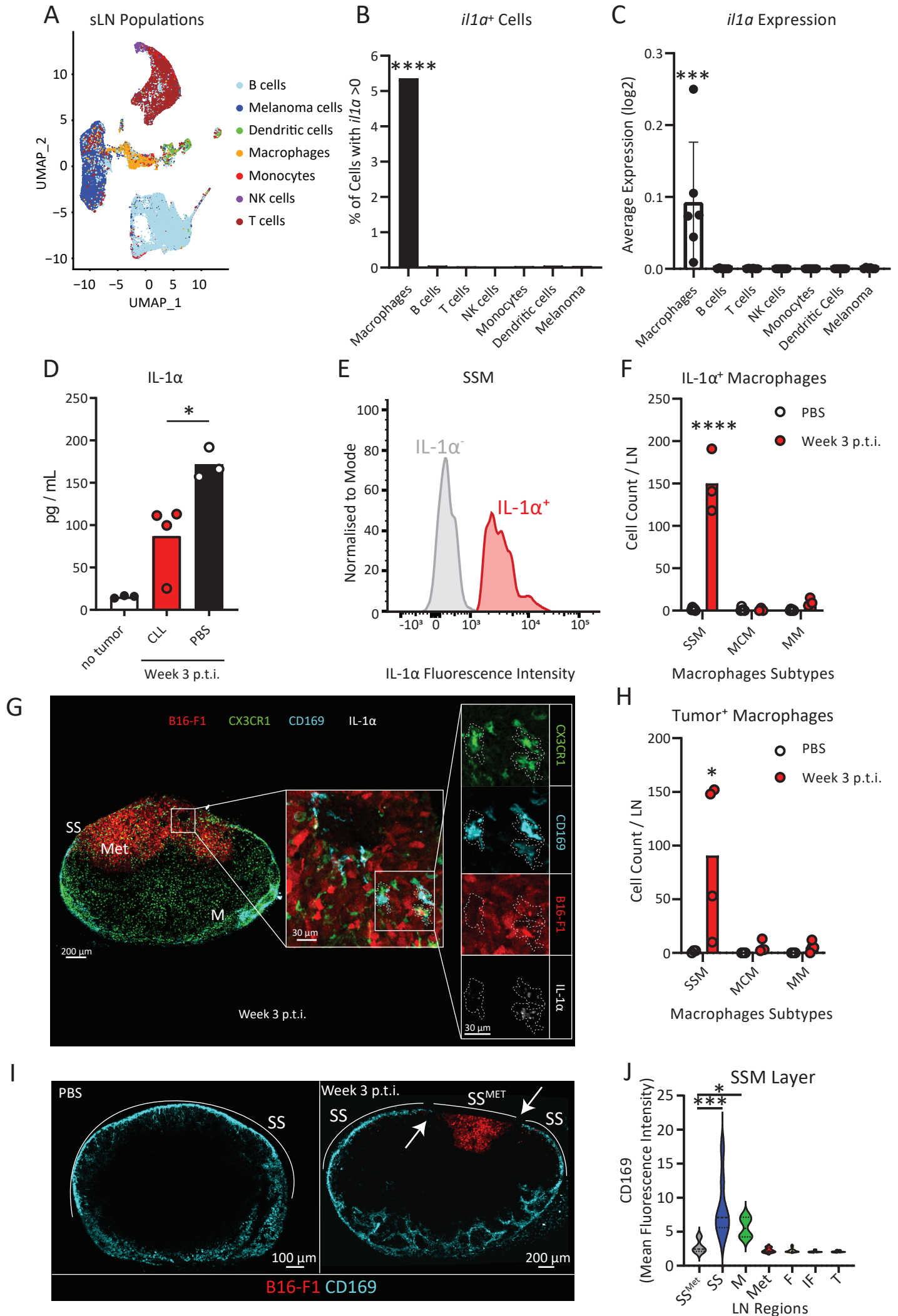
Figure 4. SSM derived IL-1α directly supports tumor proliferation

A
IL-1R1 Expression

B
Metastatic Cells

C
Metastasic Ratio

D
Proliferation Assay
B16-F1 (Mouse)

E
Proliferation Assay
A3775 (Human)

F
MYD88

Figure 5: IL-1α induces STAT3 expression and phosphorylation in tumor.